Impact of Feed Rate and Binder Concentration on the Morphology of Spray Dried Alumina-Polymer Nanocomposites

Rahul Mitra[a,*], Lukas Fuchs[b], Orkun Furat[b], Yannik Sinnwell[c], Sergiy Antonyuk[c], Volker Schmidt[b], Urs A. Peuker[a]

[a]*Institute of Mechanical Process Engineering and Minerals Processing, TU Bergakademie Freiberg, Agricolastr. 1, Freiberg, 09599, Saxony, Germany*
[b]*Institute of Stochastics, Ulm University, Helmholtzstr. 18, Ulm, 89069, Baden-Württemberg, Germany*
[c]*Institute of Particle Process Engineering, University of Kaiserslautern-Landau (RPTU), Gottlieb-Daimler-Straße 74, Kaiserslautern, 67663, Rhineland-Palatinate, Germany*

Abstract

Spray drying is a versatile technique for producing fine powders with controlled size and morphology. This study investigates the impact of both feed rate and binder concentration on the morphology and porosity of the spray-dried powder of nano-alumina and polyvinylpyrrolidone (PVP-30) granules. Droplet size and velocity distributions, measured using HiWatch setup, indicated that higher feed rates generate larger droplets with increased velocities, directly influencing the resultant three-dimensional (3D) morphology of the dried product. The morphology of the dried granules was analyzed using in-line SOPAT imaging. Off-line scanning electron microscopy (SEM) was also used to characterize the morphology of the dried product, while pore volume and pore size of the granules was quantified by mercury intrusion porosimetry. The results indicate that higher feed rates lead to larger granules and larger pore volumes, whereas increasing the binder concentration yields a more compact morphology with reduced pore volume. By understanding the relationship between these process parameters and product characteristics, this research contributes to the optimization of spray drying processes for the production of high-quality alumina–polymer nanocomposites.

Keywords: Spray drying, Optimization, Process-product relationship, Polymer composite, Particle technology, Image processing, Parametric stochastic modeling

1. Introduction

Polymer nanocomposites possess a wide range of industrial uses, e.g., in biomedicine, pharmaceuticals, electronics and ceramics [1, 2, 3]. In these materials, a polymer matrix is filled with nano-particles [4, 5, 6] that enhance the mechanical, magnetic, electrical or optical properties [6, 7, 8, 9, 10, 11]. A key challenge in fabricating such composites is preventing the agglomeration of nano-particles, since van der Waals forces and other attractive interactions are relatively strong at the nanoscale [7, 9, 10, 12, 13]. Over the years, various synthesis routes have been developed to achieve a homogeneous dispersion of nano-particles within polymers. These include: (1) synthesizing nano-particles and polymers separately and then mixing them (e.g., in a melt or solution), (2) in-situ generation of nano-particles within a polymer matrix, and (3) polymerizing monomers around dispersed nano-particles [7, 8, 14]. Each method has advantages; however,

*corresponding author
Email address: Rahul.Mitra@mvtat.tu-freiberg.de (Rahul Mitra)

many fail to achieve uniform dispersion of nano-particles when incorporating high concentrations of nano-particle fillers [8, 9, 12].

Spray drying is a process where a liquid containing dispersed solids is atomized into droplets from a nozzle, leading to solidification through concentration increase in the presence of circulating drying gas [15]. The atomization process of the liquid into droplets is one of the relevant factors that affects the properties of the dried product [16]. Spray drying a polymer solution containing pre-dispersed nano-particles has emerged as an effective method to create polymer nanocomposites. In the process developed by Banert and Peuker [4], a solution of polymer and nano-particles is spray-dried to produce a composite material with uniform nano-particle distribution. This method takes advantage of a low-viscosity solvent to disperse nano-particles, with polymer molecules adsorbing on nano-particle surfaces to provide steric stabilization against aggregation [9, 17]. The rapid evaporation of the solvent in the spray dryer "freezes" the dispersed state, preventing nano-particle agglomeration during solidification [8]. Previous studies have successfully applied this solution-spray-drying approach to create polymer composites highly loaded with magnetite and other nano-materials [18, 19].

Nano-alumina (nano-Al_2O_3) filled polymer composites have gained significant attention in recent years due to their exceptional properties and applications. Such alumina-polymer nanocomposites combine the high strength, thermal stability, and wear resistance of alumina with the flexibility and process ability of polymers. They are being explored for uses in catalysis, battery electrodes, and drug delivery, among others [20, 21, 22, 23, 24]. The spray drying method provides a promising route to synthesize these nanocomposites, as it allows precise control over the dried product properties such as size, morphology, and internal structure [25, 26, 27, 28]. However, systematic studies on how spray drying process parameters affect the morphological and structural characteristics of dried products are required to guide process optimization. A deeper understanding of these relationships is essential for the effective application of model-based control strategies, which are central to our research goal.

In this experimental study, we spray dry a suspension of nano-alumina and polyvinylpyrrolidone (PVP-30) in water to produce alumina–polymer nanocomposite. The composite product material is an granule formed from the primary alumina nano-particles with PVP-30 particles acting as bridges. The focus of the experimental investigation is the examination of the effect of two critical process parameters: (a) the feed rate (the liquid feed flow rate into the dryer) and (b) the binder concentration (the mass fraction of PVP-30 in the liquid feed) on the resultant size, shape, and porosity of the dried granules. All other process parameters are held constant to isolate the effects of these two concerned parameters.

We employ an in-line imaging probe (SOPAT imaging system) to capture the granule morphology, which has been used already to study particle morphologies and agglomeration [29, 30]. To obtain detailed insights into the granule morphology, off-line characterization techniques are carried out on the granules. High-resolution scanning electron microscopy (SEM) characterization is conducted on the spray-dried product to visualize the rich structures of the granules, followed by mercury intrusion porosimetry [31] to quantify the internal porosity of the dried granules. By correlating the morphological observations from the in-line SOPAT data with the off-line porosity data, we seek a deeper understanding of the relationship between feed rate and binder concentration, granule size/shape, and pore volume/size.

This approach aligns with the growing trend towards model-based control of spray drying processes [32, 33], where understanding the relationships between process parameters and product characteristics is crucial for developing predictive models [34] and control strategies [35, 36]. In particular, parametric stochastic modeling approaches have been deployed to derive interpretable

relationships that allow for the predictive simulation of products [37, 38] at unseen scenarios, as well as for the optimization of products by optimizing process parameters [39]. Such an approach can dynamically predict and adjust process conditions in real-time, enabling the consistent production of tailored particle properties for specific application requirements. Thus, our study contributes to the understanding of spray drying process depending on the process parameters and establishes a preliminary pathway towards automated and optimized control of such processes.

The present paper is structured as follows. Section 2 details the materials and methods employed in the study, covering the characteristics of feed materials, the experimental spray drying setup, an outline of all the spray drying experiments conducted in this investigation, the droplet characterization setup, image processing algorithms, and the definitions of size and shape descriptors utilized for granule characterization. The section concludes with an introduction to the mathematical basis of the parametric modeling and prediction analysis discussed later in Section 3.2. Section 3 presents experimental results, including droplet characterization, granule size and shape descriptor distributions, SEM analyses, and mercury intrusion porosimetry measurements. Specifically, the section explores how variations in feed rate and binder concentration affect: (a) droplet size and velocity distributions during atomization, (b) size and shape descriptor distributions of dried granules, and (c) the pore volume and pore size distributions within the granules. A parametric statistical analysis is applied to model granule size and shape descriptor distributions based on process parameters. Section 4 provides an in-depth discussion of the experimental findings from Section 3, offering explanations for observed phenomena based on fundamental physical principles and microstructural observations. Finally, Section 5 summarizes the key findings and discusses their implications for the optimized design and production of spray-dried alumina–polymer composites.

2. Material and methods

2.1. Feed material

The primary solid component used in the spray drying experiments was spherical alumina powder (DENKA Alumina ASFP-20). These alumina nano-particles have a well-defined spherical morphology and a solid, non-porous structure, as confirmed by SEM imaging of the raw, unprocessed powder (Figure 1a). The absence of internal voids or surface cracks in the as-received particles ensures a uniform starting material, which is crucial for attributing any changes in morphology solely to the spray drying process. To characterize the size of the alumina nano-particles, we performed dynamic light scattering (DLS) measurements using a Sympatec Nanophox analyser. The DLS measurements provided the particle size distribution in suspension. The empirical cumulative size distribution and probability density distribution acquired by the DLS measurements are shown in Figure 1b. It is important to note that Figure 1 represents a number-weighted distribution, meaning each detected particle in the suspension contributes equally to the overall distribution. In other words, the resulting cumulative or density distribution reflects the relative abundance of particles of a given diameter, rather than emphasizing the mass or volume. The alumina nano-particles have a median diameter ($d_{50,0}$) of approximately 0.368 µm and a modal diameter ($d_{h,0}$) of 0.356 µm.

In order to perform spray drying experiments, a liquid feedstock was prepared as an aqueous suspension of the alumina nano-particles with dissolved PVP-30 as a binder. In a typical batch, 33.3 g of ASFP-20 alumina powder and 2.67 g of PVP-30 were mixed into 300 mL of distilled water. This corresponds to a solids content of 10 wt% alumina and 0.8 wt% PVP-30 in the suspension. The PVP-30 acts as a polymeric binder which, after drying, helps to hold the alumina nano-particles together in the composite. To investigate the influence of binder concentration, even further liquid feedstocks were prepared with PVP-30 mass fractions of 0.4 wt%, 1.6 wt%, and 3.2 wt%, while

keeping the alumina content fixed at 10 wt%. Each feedstock was freshly prepared before every experimental case listed in Section 2.3 to ensure consistency and to avoid any effects of aging or sedimentation.

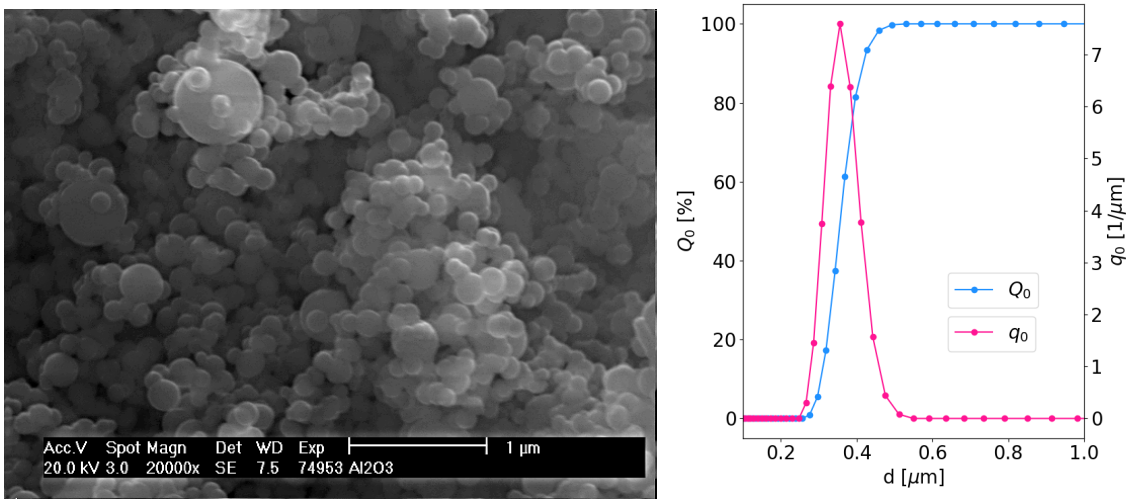

(a) (b)

Figure 1: a) SEM micrograph of ASFP-20 alumina nano-particles; (b) Number-weighted cumulative distribution function (blue) and probability density function (red) of particle size obtained from DLS measurements.

2.2. Experimental setup

The BÜCHI B-290 Mini Spray Dryer, a laboratory-scale instrument, was employed for conducting the spray drying experiments. This particular instrument features a standard two-fluid nozzle, characterized by a diameter of 0.7 mm and a nozzle cap diameter of 1.4 mm, which facilitates the efficient atomization of the liquid feed into fine droplets.

The atomization process utilizes compressed air, functioning as the spray gas, with adjustable flow rates ranging from 200 L h^{-1} to 800 L h^{-1} and operating pressures between 5 bar and 8 bar. This inherent flexibility in the system allows for control over the formation of droplets and their corresponding size distribution.

The drying gas, typically air, is heated to a maximum inlet temperature of 220 °C, which is accurately measured by a PT-100 thermocouple with a control accuracy of ±3 °C, ensuring consistent thermal conditions for effective drying. The evaporative capacity of the instrument is rated at 1 L h^{-1} specifically for water. The aspirator component is responsible for generating the drying gas flow, with a maximum airflow capacity of 35 m^3 h^{-1}, providing sufficient residence time, ranging from 1 s - 1.5 s, for the droplets to undergo complete drying within the chamber.

The liquid feedstock is introduced into the nozzle by means of a peristaltic pump, which offers adjustable flow rates up to 30 mL min^{-1}. The BÜCHI B-290 Mini Spray Dryer incorporates an integrated cyclone separator positioned at the outlet of the drying chamber, efficiently collecting the dried product and minimizing any potential product loss. The transparent glass assembly of the instrument provides visual access to the spray drying process, facilitating real-time monitoring and adjustments during operation. A labeled view of the entire experimental setup, including the attached SOPAT imaging probe, is illustrated in Figure 2.

2.3. Conducted spray drying experiments

Using the materials and setup described above, we performed a series of spray drying experiments to systematically study the effect of feed rate and binder concentration. Four experiments were

conducted with varying feed rates (referred to as "F series") while keeping the binder concentration constant at 0.8 wt% (PVP-30) and all other operating parameters fixed (as listed in Table 1). These experimental cases are labeled F1B2, F2B2, F3B2, and F4B2, corresponding to feed flow rates of 11, 14, 17, and 20 mL min^{-1}, respectively. In each experimental case, the atomization pressure (5 bar), spray gas flow (742 L h^{-1}), inlet temperature (220 °C) and drying gas flow (35 m^3 h^{-1}) were held constant. By comparing the experimental cases of the F series, the isolated impact of increasing feed rate on the product properties can be observed.

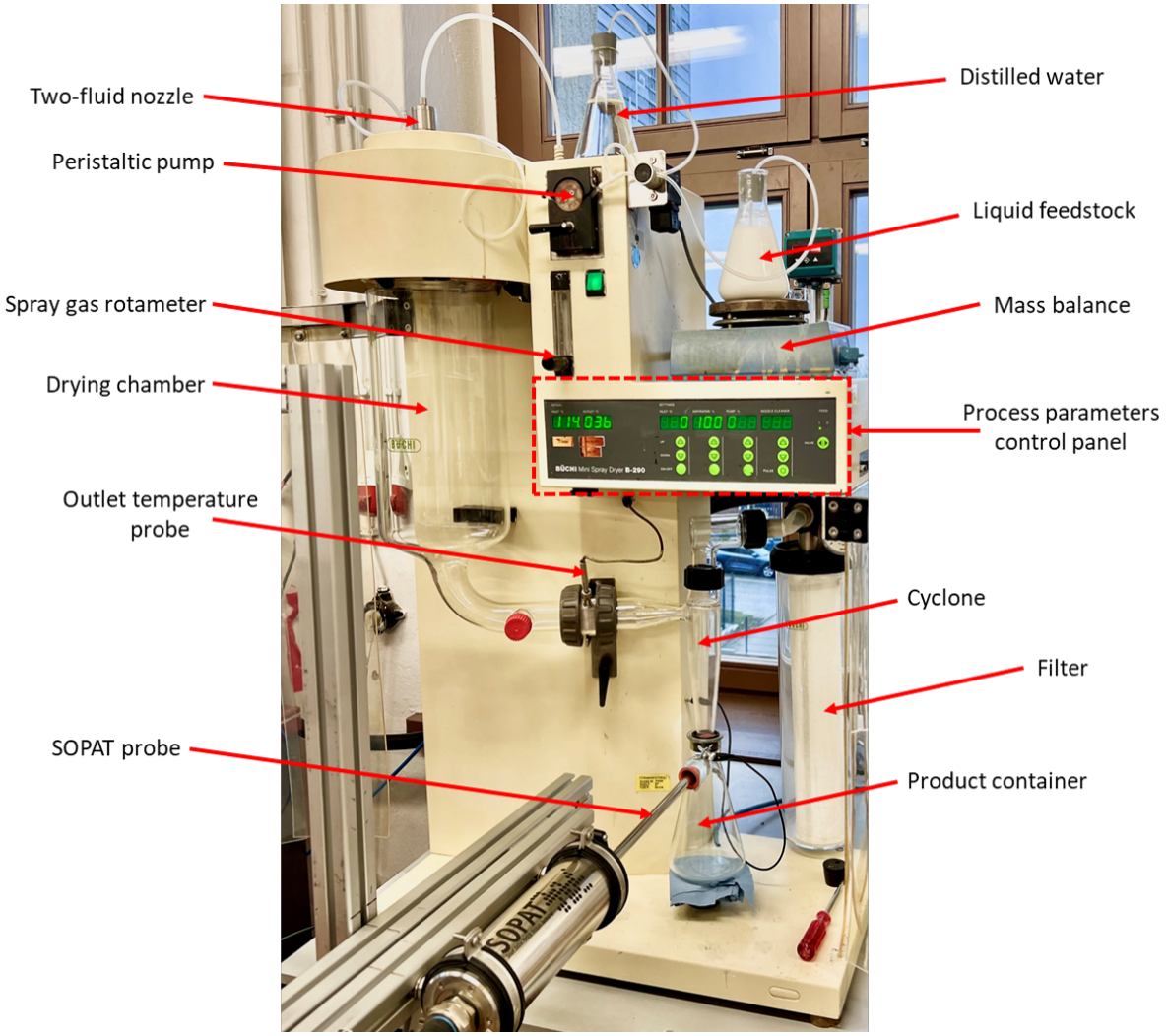

Figure 2: Photograph of the spray drying setup with the integrated SOPAT in-line imaging probe.

Next, to examine the influence of binder concentration, three additional experiments were carried out at the lowest feed rate (11 mL min^{-1}) while varying the PVP-30 concentration (referred to as "B series"). These cases are labeled F1B1, F1B3, and F1B4, which used 0.4 wt%, 1.6 wt%, and 3.2 wt% PVP-30 (by mass), respectively. All other process parameters in F1B1, F1B3, and F1B4 were identical to the process parameters of the F series experimental cases (see Table 1) so that the effect of the binder fraction on the product properties could be isolated.

Each experimental case was performed with a fresh batch of liquid feedstock and ran until enough product was collected for analysis (several grams of dried powder). The in-line SOPAT imaging was conducted during each spray run to capture images of the granules under steady-state conditions (after drying), and samples of the powder were later taken for porosity measurements.

Table 1: Summary of spray drying experimental conditions (fixed parameters and variable settings). The experimental cases denote feed rate (F1=11, F2=14, F3=17, F4=20 mL min^{-1}) and binder concentrations (B1=0.4 wt%, B2=0.8 wt%, B3=1.6 wt%, B4=3.2 wt%).

Process parameters	**F series**				**B series**		
	F1B2	**F2B2**	**F3B2**	**F4B2**	**F1B1**	**F1B3**	**F1B4**
Atomization pressure [bar]	5	5	5	5	5	5	5
Spray gas flow rate [$\mathrm{L\,h^{-1}}$]	742	742	742	742	742	742	742
Inlet temperature [°C]	220	220	220	220	220	220	220
Drying gas flow rate [$\mathrm{m^3\,h^{-1}}$]	35	35	35	35	35	35	35
Feed flow rate [$\mathrm{mL\,min^{-1}}$]	11	14	17	20	11	11	11
PVP-30 concentration [wt%]	0.8	0.8	0.8	0.8	0.4	1.6	3.2

2.4. Off-line droplet imaging setup

In order to link the spray drying conditions to the resulting product formation, it is important to first understand how the liquid feed breaks up into droplets under different feed rates and binder concentrations. Therefore, we employed an optical spray characterization system (Oseir Ltd. HiWatch HR2) to measure the droplet size and velocity distributions in the spray. This system was used independently of the B-290 dryer (on a separate setup) to replicate the atomization conditions and gather detailed droplet data.

The HiWatch HR2 system uses a backlight illumination and a high-speed camera to capture images of droplets, applying a particle tracking velocimetry (PTV) technique. A multi-pulse laser illumination during a single camera exposure creates multiple faint "shadow" images of each droplet in motion. In essence, each droplet appears as a series of three closely spaced silhouettes (a shadowing triplet) in the image, corresponding to successive laser pulses. By detecting these triplets, the system can determine an individual droplet's velocity (from the spacing of the silhouettes) and size (from the size of the silhouettes) simultaneously [40] – an approach termed as sizing PTV (S-PTV).

A schematic of the HiWatch optical setup is shown in Figure 3. The HiWatch is capable of sizing droplets down to 5 µm in diameter. For our measurements, the laser was configured to emit a train of three pulses with a fixed interval of 25 ns between pulses. This produced the shadow triplets needed for velocity calculation. We adjusted the pulse frequency and camera exposure such that droplets with velocities up to the expected maximum could be accurately tracked. Each measurement was conducted for 120 s to 240 s, capturing spray data (depending on when a sufficient number of droplet images was collected). All droplet measurements were performed at a position 50 mm below the nozzle.

To extract quantitative data, the raw images from the HiWatch system underwent a processing algorithm provided by the manufacturer. First, a pre-processing step removed background noise (e.g., static reflections) to enhance the triplet detection. Then, the software identified groups of three collinear droplet shadows and linked them as triplets based on consistent spacing. Any spurious or overlapping signals that could not be unambiguously assigned to triplets were filtered out via morphological operations and autocorrelation analysis. This ensured that only true droplet signals were used for calculating velocities. The outcome of this procedure is a set of droplet diameters and velocities for each condition tested.

To characterize the droplet size and velocity distributions, we applied Gaussian kernel density estimation (KDE) to each dataset, which is a non-parametric method for estimating a probability density function (PDF) of a random variable [41]. We then integrated the resulting PDFs to obtain the corresponding cumulative distribution functions (CDFs). These droplet size and velocity distri-

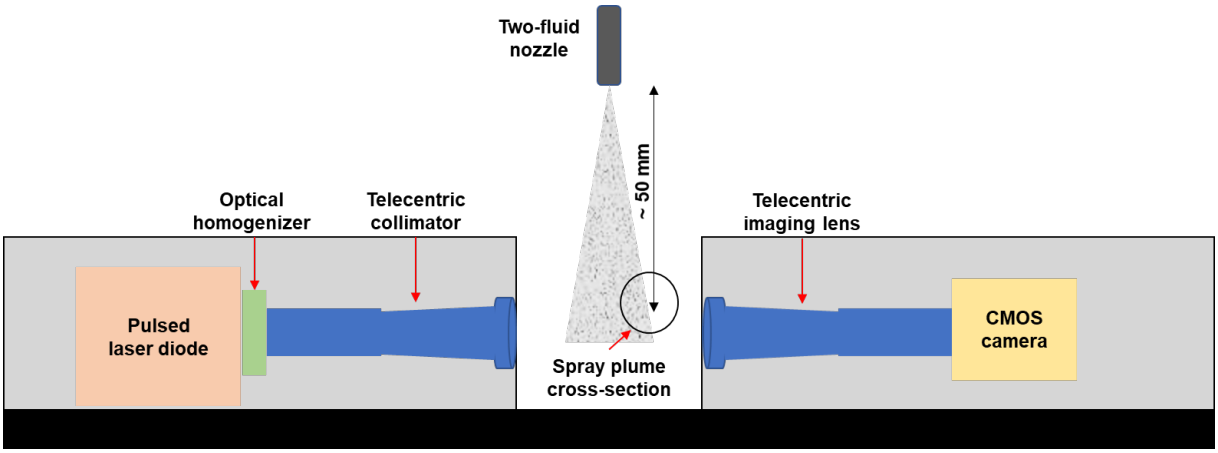

Figure 3: Schematic illustration of the HiWatch droplet imaging system setup.

butions (see Section 3.1) subsequently guided our interpretation of granule formation, as discussed in Section 3.2.

However, it should be noted that there are practical limits to the conditions we could measure. At higher feed rates or high binder concentrations, the spray becomes so dense that the HiWatch measurements are not reliable. In such regimes, the overlapping of droplet images (due to high number density and turbulence in the spray cone) makes it challenging for the S-PTV system to distinguish individual droplets. One can attempt to mitigate this by increasing the distance between the measurement zone and the nozzle, while focusing the laser beam on the edge of the spray plume, where droplet density is lower. However, the measurement region of the HiWatch has a maximum horizontal length of 8 mm that limits the vertical distance between the measurement zone and the nozzle since the spray cone cross-section increases as the vertical distance increases below the nozzle. Moreover, for the extreme case of very high feed rate and high binder concentration, quantitative droplet data cannot be obtained because of pervasive signal overlap and clustering of droplets. These constraints highlight the complex interplay of feed rate and liquid properties (viscosity, solids content) in two-fluid nozzle atomization. In dense sprays, multiple droplet interactions and rapid coalescence or trajectory perturbations can occur, complicating the measurement.

2.5. In-line granule imaging setup

To observe the dried granules produced in the spray dryer, we utilized an in-line imaging probe "SOPAT PL" from SOPAT GmbH. The in-line camera system features a long, immersible shaft with a diameter of 12 mm, which was inserted directly into the collection vessel beneath the cyclone (as illustrated in Figure 2) to capture in situ images of the granules after drying. The camera tip is equipped with a sapphire lens, ensuring durability against the abrasive alumina nano-particles. A rhodium reflector can be positioned at a distance ranging from 1 µm to 1000 µm from the camera lens. The combination of this reflector and the built-in strobe provides uniform illumination of the granules. Optimal image quality is achieved when the reflector is placed close to the lens. However, for certain material systems, a larger reflector-lens distance is preferable to prevent granules from obstructing the field of view and to accommodate larger objects. In this study, the distance between the reflector and the lens was maintained at approximately 1 mm.

The probe features a microscopic optics system with a diagonal field of view of 800 µm, capable of resolving granules in the approximate size range of 2 µm to 300 µm. Consequently, the SOPAT camera is expected to primarily capture granules formed after drying, rather than the individual primary alumina nano-particles, which are likely too small to be effectively observed.

The imaging conditions for the SOPAT probe are summarized in Table 2. The camera captured 8-bit monochrome images at a resolution of 2464×2056 pixels. With a calibrated spatial conversion factor of 0.2464 µm/pixel, this setup provides a scaling to enable accurate conversion from pixel measurements to real granule dimensions. To obtain a statistically significant size distribution at a given time t, a single image is insufficient. Instead, 100 images were acquired per measurement point at a constant frame rate of 20 Hz. The selection of the frame rate is crucial and must be adapted to the velocity of the granules being captured. If the frame rate is too high, the same granule may appear in multiple frames, potentially biasing the statistical analysis and leading to inaccuracies in the derived size distribution. The focus was adjusted to approximately 100 µm in front of the probe lens, optimizing clarity for granules at that distance. By collecting a series of images from this probe for each experimental run, we obtained datasets for image analysis to determine granule size and shape descriptor distributions (using the descriptors defined in the following Section 2.6).

Table 2: Image capture specifications for the SOPAT in-line granule imaging probe.

Image format	Monochromatic 8-bit
Image dimensions [pixels×pixels]	2464 × 2056
Frame rate [Hz]	20
Conversion factor [µm/pixel]	0.2464
Focus position [µm]	99.8629
Strobe intensity [%]	100
Exposure time [µs]	6400
Reflector distance [µm]	1000

2.6. Size and shape descriptors of granules

To quantitatively characterize the size and shape of the dried granules, we consider two key size and shape descriptors derived from two-dimensional (2D) image analysis of SOPAT images:

1. Maximum Feret diameter ($d_{\mathrm{F}_{\max}}$) – the longest distance between two parallel lines tangential to the 2D silhouette of the granule as observed in the imaging plane. It provides an estimate of the granule's largest dimension in the image plane. Formally, it is defined as

$$d_{\mathrm{F}_{\max}} = \max_{\theta\in[0,\pi)} d_{\mathrm{F}}(\theta), \tag{1}$$

   where $d_{\mathrm{F}}(\theta) > 0$ represents the distance between two distinct parallel lines at an angle θ to the x-axis that are tangents of the granule's 2D silhouette.
2. Aspect ratio (Ψ_{A}) – the aspect ratio is defined as the ratio of the minimum Feret diameter to the maximum Feret diameter ($d_{\mathrm{F}_{\max}}$) of the granule, where the minimum Feret diameter $d_{\mathrm{F}_{min}}$ is given by Eq. (1), by substituting $\max_{\theta\in[0,\pi)}$ by $\min_{\theta\in[0,\pi)}$. Then the aspect ratio Ψ_{A} is then given by

$$\Psi_{\mathrm{A}} = \frac{d_{\mathrm{F}_{min}}}{d_{\mathrm{F}_{max}}}. \tag{2}$$

   Note that the aspect ratio is a dimensionless number between 0 and 1 that indicates the compactness or elongation. An aspect ratio of 1 indicates a compact shape (equal length and width), whereas values significantly less than 1 indicate an elongated 2D silhouette.

A schematic representation of the minimum and maximum Feret diameters is shown in Figure 4 for an irregularly shaped solid. These two descriptors ($d_{\mathrm{F}_{\max}}$ and Ψ_{A}) together provide a simple but

effective characterization of the granule's morphology. In subsequent analysis, we will use them to compare the effects of different process parameters (feed rate and binder concentration) on the size distribution and shape uniformity of the granules.

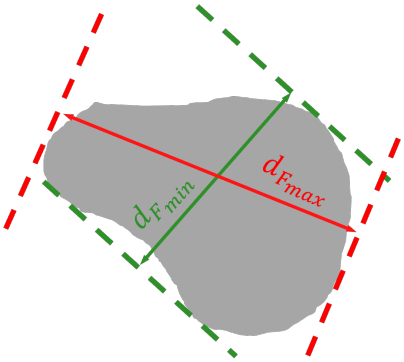

Figure 4: Schematic representation of the minimum and maximum Feret diameters for an irregularly shaped solid.

2.7. In-line image processing pipeline

The raw images of dried product from the SOPAT probe were analyzed through an image processing pipeline to detect the granules and measure their descriptors ($d_{\mathrm{F_{max}}}$ and Ψ_{A}). An example illustrating the key steps of this pipeline is provided in Figure 5. First, each raw image (Figure 5a) is loaded along with the calibrated pixel-to-micron conversion factor from the automatically generated log-file during image acquisition. To enhance granule visibility, we apply local background subtraction. To do so, for each image, a background intensity image is estimated (precisely, by taking a moving median filter over a 2D neighborhood of 51×51 pixels around each pixel) that is then subtracted from the original image [42]. This operation improves clarity by removing uneven illumination and static artifacts, making the granules stand out. Then, we then perform contrast-limited adaptive histogram equalization (CLAHE) to further enhance image contrast [43]. CLAHE operates on small regions (tiles) of the image, equalizing the histogram within each tile but limiting the contrast amplification to avoid noise enhancement. This technique is particularly useful for bringing out faint edges of granules without over-saturating noise in dark areas. We also apply a bilateral filter [44] to reduce high-frequency noise while preserving the edges of the granules. The bilateral filter replaces each pixel with a weighted average of its neighbors, where weights depend on both spatial proximity and intensity similarity. After these steps (illustrated in Figures 5b–c), granules appear much clearer against the background.

The pre-processed image is then converted to a binary (black-and-white) image to segment the granules. We use Otsu's global thresholding method [45] to automatically choose an intensity threshold that separates foreground (granules) from background. Pixels above the threshold are set to white (granule) and below to black (background). This yields an initial binary mask (Figure 5d). Next, we apply morphological operations to clean up the segmentation. In particular, we use a morphological opening operation (erosion followed by dilation) to remove tiny white specks (noise) and to smooth the boundaries of granule regions. The result is a refined binary image where each white region corresponds to an granule (Figure 5e).

Finally, connected-component labeling is performed on the binary image to identify individual regions. Each region is considered to be one detected granule (Figure 5f). For each region, we compute the size and shape descriptors: the maximum Feret diameter $d_{\mathrm{F_{max}}}$ and aspect ratio Ψ_{A}, as defined in Section 2.6.

We intentionally kept this segmentation algorithm straightforward and computationally light so that it could be used to process in-line measurements in near real-time. Despite its simplicity, the algorithm achieved high accuracy in identifying the granules correctly and then calculate their size and shape. We validated the image analysis by manually hand-labeling a subset of granules (see, for example, Figures 5g-i) and comparing the descriptors computed for hand-labeled and algorithmically segmented granules, see Table 3. This level of accuracy was deemed sufficient for reliable analysis of trends in granule size and shape.

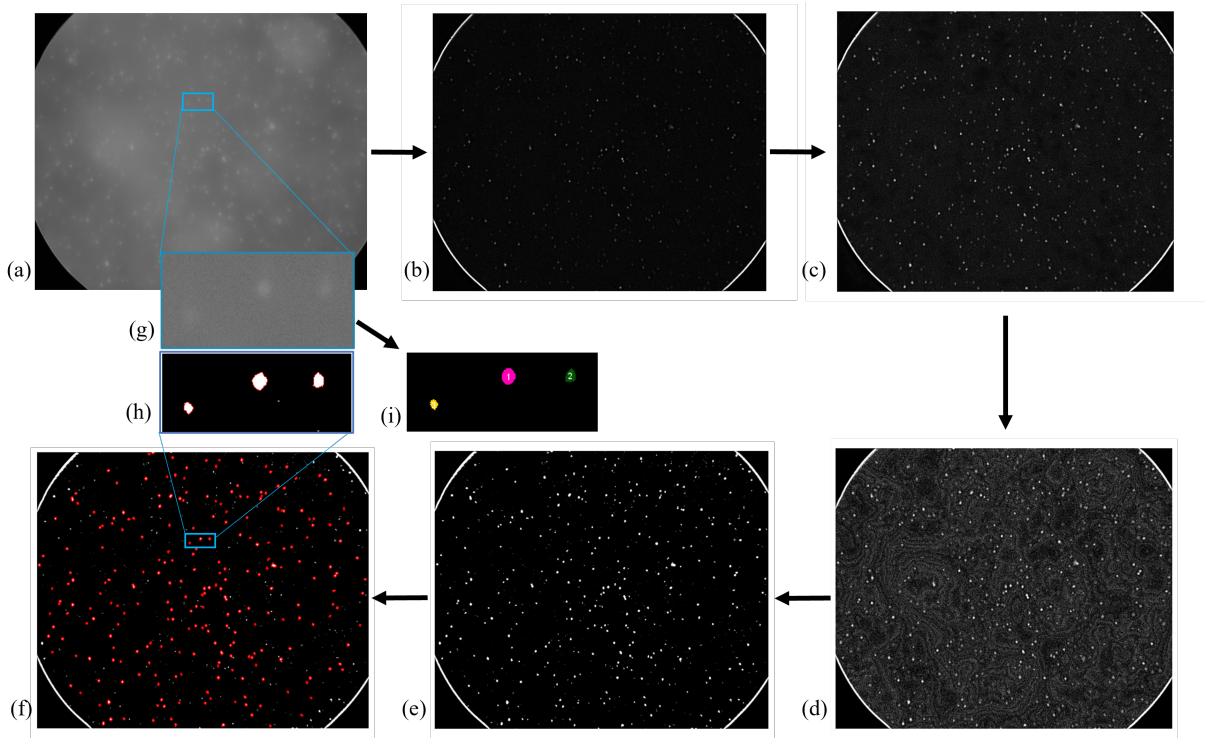

Figure 5: Example of granule detection workflow from SOPAT images: (a) raw image, (b) after background removal, (c) contrast enhancement and bilateral filtering, (d) Otsu thresholding, (e) morphological operations, (f) final granule detection, (g) zoomed-in view of raw image section, (h) corresponding zoomed-in detected granules, and (i) manual labeling of granules from image (g). The overall contrast and sharpness of the images (a-c) was increased by 20% and 100%, respectively, for the sake of better visibility in this paper.

Table 3: Segmentation validation for three example granules, comparing hand-labeled (HL) measurements vs. automated (AL) image analysis.

Label	$\boldsymbol{d_{\mathbf{F_{max}}}}$ (HL) [µm]	$\boldsymbol{d_{\mathbf{F_{max}}}}$ (AL) [µm]
1	4.99	4.99
2	4.35	4.16
3	3.25	3.08

Label	$\boldsymbol{\Psi_A}$ (HL) [-]	$\boldsymbol{\Psi_A}$ (AL) [-]
1	0.79	0.79
2	0.66	0.63
3	0.72	0.68

2.8. Parametric modeling and prediction of descriptor distributions

We employ parametric modeling to allow for the straightforward and easy comparison of granule descriptor distributions measured for different experimental cases. For that let $A_1, \ldots, A_n \subset \mathbb{R}, n > 1$ be the (finite) data sets of granule descriptors measured in processes with parameters $z_1, \ldots, z_n \in \mathbb{R}$. By considering a parametric family of probability densities $\{f_\theta, \theta \in \Theta\}$ and fitting densities $f_{\theta_1}, \ldots, f_{\theta_n} \colon \mathbb{R} \to [0, \infty)$ to these data sets, we achieve a low-dimensional representation of the data sets in terms of the model parameters $\theta_1, \ldots, \theta_n \in \Theta \subset \mathbb{R}^m$ for some integer $m \geq 1$. This low-parametric representation offers several advantages over non-parametric techniques, such as KDEs, which are simple to implement and do not require any assumption on the data. However, parametric modeling provides some key advantageous, such as interpretability, dimensionality reduction and computational efficiency. These benefits are especially important in applications like on-line process monitoring. By determining a functional relationship between the process parameters $z_1, \ldots, z_n \in \mathbb{R}$ and the model parameters $\theta_1, \ldots, \theta_n \in \Theta$ by means of regression, we can predict model parameters, and thus descriptor distributions, for not yet conducted experiments.

For a given family of parametric probability densities $\{f_\theta, \theta \in \Theta\}$, the optimal parameters $\theta_1^*, \ldots, \theta_n^*$ associated with the process parameters $z_1, \ldots, z_n$ can be determined by means of maximum likelihood estimation [46]. Therefore, we consider the likelihood function $\mathcal{L} \colon \Theta^n \to \mathbb{R}$ which is given by

$$\mathcal{L}(\theta_1, \ldots, \theta_n) = \prod_{i=1}^{n} \prod_{x \in A_i} f_{\theta_i}(x), \tag{3}$$

for any $\theta_1, \ldots, \theta_n \in \Theta$. Then, the optimal parameter values $\theta_1^*, \ldots, \theta_n^* \in \Theta$ can be determined by maximizing the likelihood function considered in Eq. (3), $\mathcal{L}$, i.e.,

$$(\theta_1^*, \ldots, \theta_n^*) = \underset{(\theta_1, \ldots, \theta_n) \in \Theta^n}{\operatorname{argmax}} \mathcal{L}(\theta_1, \ldots, \theta_n). \tag{4}$$

When considering more than one parametric family of probability densities, the family leading to the best fit can be identified by choosing the family that yields the largest likelihood value $\mathcal{L}(\theta_1^*, \ldots, \theta_n^*)$, i.e., the family for which the value of $\max_{(\theta_1, \ldots, \theta_n) \in \Theta^n} \mathcal{L}(\theta_1, \ldots, \theta_n)$ is highest.

For predicting the probability density of the descriptor under consideration for a process with process parameter z for which no data were acquired yet, we utilize a parametric regression function $g \colon \mathbb{R} \to \Theta$, which maps the process parameter $z \in \mathbb{R}$ to a model parameter $\theta = g(z) \in \Theta$ of the desired probability density $f_{g(z)}$. In the present paper we consider a linear regression function g given by

$$g(z) = a \cdot z + b, \tag{5}$$

for each $z \in \mathbb{R}$, where $a, b \in \mathbb{R}^m$ are parameters that have to be fitted to data. More precisely, optimal parameter values $a^*, b^* \in \mathbb{R}^m$ are determined by means of a mean-squared error-based regression between $z_1, \ldots, z_n$ and $\theta_1^*, \ldots, \theta_n^*$, i.e.,

$$(a^*, b^*) = \underset{a, b \in \mathbb{R}^m}{\operatorname{argmin}} \frac{1}{n} \sum_{i=1}^{n} (g(z_i) - \theta_i^*)^2. \tag{6}$$

3. Experimental Results

In the following, we present the experimental results obtained for the process scenarios outlined in Section 2.3. The findings are organized as follows: we first examine the droplet characteristics (Section 3.1), then analyze the distributions of size and shape descriptors for dried granules (Section 3.2), including statistical modeling of the distributions. This is followed by a discussion of qualitative observations from SEM imaging (Section 3.3) and, finally, a quantitative analysis of porosity (Section 3.4). This structure allows us to build a comprehensive understanding from the spray formation through to the final product properties.

3.1. Droplet size and velocity distribution

To understand the influence of feed rate and binder concentration on the atomization process, we first analyzed the size and velocity distributions of the droplets produced by the two-fluid nozzle under different values of the concerned process parameters. Using the HiWatch S-PTV system, already described in Section 2.4, we obtained droplet data for selected representative experimental cases: a low feed rate with low binder (F1B1), a low feed rate with high binder (F1B2) and a high feed rate with high binder (F2B2). It was not possible to obtain analyzable data for the other experimental cases with higher feed rate or binder concentrations due to the signal overlapping constraint discussed in Section 2.4. The resulting PDFs and CDFs are plotted in Figure 6 for the size and velocity, respectively.

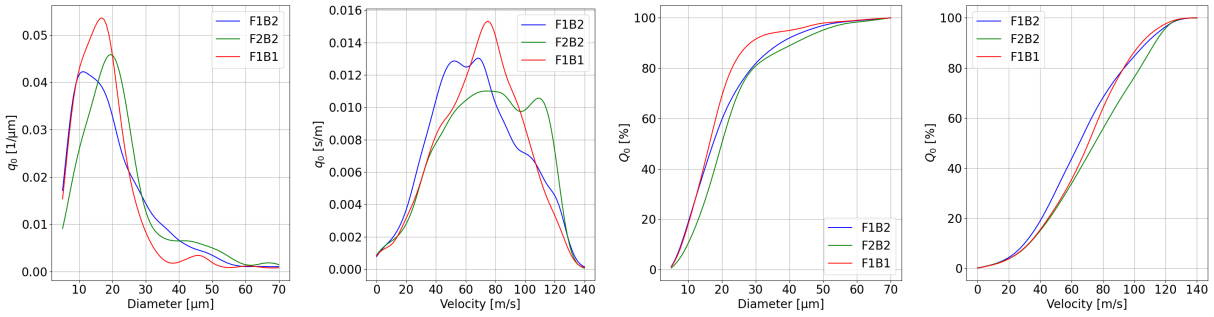

(a) PDF size (b) PDF velocity (c) CDF size (d) CDF velocity

Figure 6: PDFs and CDFs for droplet size (a,c) and velocity (b,d) from HiWatch measurements.

Droplet size. All three tested cases exhibit a unimodal droplet size distribution (Figure 6a). However, there are shifts in the distribution depending on feed rate and binder content. At a constant low feed rate (F1 series), the case with lower binder concentration (F1B1) produced droplets that are, on average, smaller than those with a higher binder content (F1B2). The peak of the probability density of the droplet size for F1B1 (in red) is located at a larger diameter than that of F1B2 (in blue), but F1B1 exhibits a steeper drop-off at larger diameters. Additionally, while F1B2 (0.8 wt% binder) has a more pronounced tail for larger droplets ($> 25\,\mu m$), F1B1 (0.4 wt% binder) shows a distribution that is more concentrated around its peak. This trend is confirmed by the cumulative size distribution functions (Figure 6c). The CDF for F1B1 lies to the left of F1B2, indicating that percentiles for the droplet size are smaller for F1B1. For example, the median droplet diameter (50^{th} percentile) is smaller in F1B1 than in F1B2. Thus, reducing the binder concentration (at low feed rate) tends to yield generally smaller droplets.

Increasing the feed rate while keeping binder the same has the opposite effect. Comparing F2B2 (in green) (high feed rate, 0.8 wt% binder) to F1B2 (in blue) (low feed rate, 0.8 wt% binder), we observe that the droplet size distribution for F2B2 is shifted towards larger diameters. The

probability density for F2B2 indicates a large variance with a noticeable tail towards large droplets, and its cumulative distribution function is located to the right of F1B2, indicating a larger median droplet size for the F2B2 case. In our measurements, the median droplet diameter increased under higher feed rates (F2B2) in comparison to lower feed rates (F1B2).

Droplet velocity. The droplet velocity data (Figures 6b and 6d) show trends associated with both feed rate and binder concentration. At low feed rate (F1), the lower binder case (F1B1) produced notably higher droplet velocities than the higher binder case (F1B2). The probability density of droplet velocity for the F1B1 case is shifted towards larger values compared to F1B2, and the corresponding cumulative distribution function shows that higher velocities are reached for the F1B1 case (its function is to the right of F1B2). This suggests that for low binder contents (and thus for lower viscosities of the liquid and possibly for lower surface tensions), the droplets emerge from the nozzle with greater speed. When the feed rate is increased (F2B2 vs F1B2, both at 0.8 wt% binder), we also see an increase in droplet velocity. The F2B2 condition yields higher velocities on average than F1B2, as evidenced by the probability density of droplet velocity being shifted rightward for the F2B2 case. Moreover, the cumulative distribution functions lies to the right for higher velocities, i.e., in comparison to the F1B2 case. The nearly monotonous trend observed in the cumulative distribution functions of droplet velocities suggest that F2B2 droplets are the fastest, followed by F1B1, and then F1B2. This hierarchy indicates that both a higher feed rate and a lower binder concentration can contribute to higher droplet exit velocities.

These trends observed from the droplet analysis provide valuable insight. They confirm that feed rate and binder concentration influence the initial droplet size/velocity, which in turn is expected to impact the product, namely, the resulting dried granules. In the following sections, we connect these findings to the properties of the dried granules. Larger and slower-evaporating droplets (from high feed rates) should yield larger dried granules with potentially more internal voids, whereas smaller, faster-drying droplets (from low feed or low binder) should produce smaller, more solid granules. The next section examines the actual size and shape descriptor distribution of the dried granules to verify these relationships.

3.2. Distributions of granule size and shape descriptors

Once the drying process was completed, the resulting granules were examined in terms of size and shape using the descriptors (stated in Section 2.6) derived from in-line SOPAT images. Figure 7a shows the number-weighted CDFs of granule size (as represented by $d_{\mathrm{F_{max}}}$) for the four different feed rates in the F series (all at 0.8 wt% binder content). The CDFs were calculated in the same way as the CDFs for the droplet size and velocity, i.e. by integrating the PDFs obtained by applying Gaussian KDE. Figure 7b presents the number-weighted CDFs of the maximum Feret diameter distribution functions for the different experimental cases of the B series.

The characteristic percentile values ($d_{10,0}$, $d_{50,0}$ and $d_{90,0}$) extracted from these CDFs for both the F series (varying feed rate) and the B series (varying binder concentration) are summarized in Table 4.

For the F series, increasing the feed rate from F1B2 to F4B2 leads to a systematic increase in granule size across all three characteristic percentiles. Specifically, the median granule size ($d_{50,0}$) increases from approximately 3.76 µm (F1B2) to 5.42 µm (F4B2), with similar trends observed at the 10^{th} and 90^{th} percentiles. This indicates that higher feed rates consistently shift the granule size distribution toward larger sizes.

Similarly, for the B series, increasing the binder concentration from F1B1 to F1B4 at a constant feed rate also increases the granule size substantially. The median size ($d_{50,0}$) increases from 3.65 µm (F1B1) to 5.35 µm (F1B4). Again, this growth trend is consistently observed at the lower

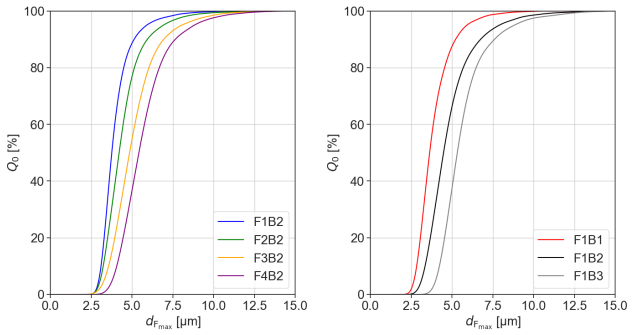

(a) F series (b) B series

Figure 7: CDFs of $d_{\mathrm{F_{max}}}$ for F series (a) and B series (b) of experimental cases.

(10^{th}) and upper (90^{th}) percentiles. Thus, higher binder content promotes larger granule formation, demonstrating that both feed rate and binder concentration independently play significant roles in influencing the size distribution of spray-dried granules.

Table 4: Characteristic percentile values ($d_{10,0}$, $d_{50,0}$ and $d_{90,0}$) from the CDF of $d_{\mathrm{F_{max}}}$ for F series and B series.

	F series				**B series**		
	F1B2	**F2B2**	**F3B2**	**F4B2**	**F1B1**	**F1B3**	**F1B4**
$\boldsymbol{d_{10,0}}$ [µm]	3.11	3.26	3.57	4.07	2.87	3.36	4.26
$\boldsymbol{d_{50,0}}$ [µm]	3.77	4.23	4.85	5.42	3.65	4.49	5.35
$\boldsymbol{d_{90,0}}$ [µm]	5.16	6.06	6.97	7.69	5.34	6.84	7.82

In the rest of this section, we will deploy parametric modeling in order to further quantify the influence of process parameters on the distribution of granule size and shape descriptors.

Parametric modeling. We applied the parametric modeling approach from Section 2.8 to model the distributions of the maximum Feret diameter $d_{\mathrm{F_{max}}}$ and the aspect ratio Ψ_{A} for both the F series and B series. Specifically, we ran the optimization procedure stated in Eq. (4) four times to fit parametric PDFs to measured maximum Feret diameters across all cases in the F series and the B series. The same procedure was applied to model the distribution of measured aspect ratio Ψ_{A} along the experimental cases of the F series and B series.

As candidates for the parametric families of distributions, we considered the normal, lognormal, beta, gamma, and Student's t-distributions [47]. The distribution of the maximum Feret diameter $d_{\mathrm{F_{max}}}$ was best approximated by lognormal distributions, which are commonly used for particle sizes due to their non-negativity and right-skewness. In contrast, the distribution of the aspect ratio Ψ_{A} was best represented by normal distributions. Recall that the probability density $f_\theta \colon \mathbb{R} \to [0, \infty)$ of a normal distribution is given by

$$f_\theta(x) = \frac{1}{\sigma\sqrt{2\pi}} \exp\left(-\frac{(x-\mu)^2}{2\sigma^2}\right), \tag{7}$$

for each $x \in \mathbb{R}$, where $\theta = (\mu, \sigma) \in \mathbb{R} \times (0, \infty)$ is its two-dimensional parameter vector. Furthermore, the probability density $f_\theta \colon (0, \infty) \to [0, \infty)$ of a lognormal distribution is given by

$$f_\theta(x) = \frac{1}{(x-c)\sigma\sqrt{2\pi}} \exp\left(-\frac{(\log(x-c)-\mu)^2}{2\sigma^2}\right) \tag{8}$$

for $x > c$, and $f_\theta(x) = 0$ for $x \leq c$, where $\theta = (\mu, c, \sigma) \in \mathbb{R}^2 \times (0, \infty)$ is its three-dimensional parameter vector.

Figure 8 provides a visualization of the fitted normal and lognormal probability densities. The corresponding values of their parameters are shown in Table 5. For the F series we see a clear shift of the PDF for $d_{\mathrm{F_{max}}}$ toward larger diameters as the feed rate increases. The variances of the probability distributions of $d_{\mathrm{F_{max}}}$ increase with the feed rate, reflecting less uniform drying of larger droplets, and thus larger range of maximum Feret diameters. In contrast, the fitted probability distributions of Ψ_{A} remain centered around the same mean (≈ 0.8) for varying feed rate (F series). A value of 0.8, indicates near-compact shapes for all feed rates, though there is a slight increase in the spread of Ψ_{A} at the highest feed rate. This suggests that at high feed rates, while most granules are still roughly compact, a few more irregular shapes appear, widening the shape descriptor distribution a bit. When considering variation in binder concentration, we also observe an increase of maximum Feret diameters (see Figure 8c) with increasing binder concentration (B series). Interestingly, for the binder variation, the variance of the aspect ratio distribution (see Figure 8d) did not increase – in fact, high binder experimental cases had similar Ψ_{A} variance as low binder, but a higher mean Ψ_{A}. In other words, higher binder made all granules a bit more compact uniformly (likely because the polymer content can form smooth coatings), rather than introducing more variability in aspect ratios. This is in contrast to the feed rate effect, where high feed increased the variability of aspect ratios slightly (perhaps due to some irregular drying outcomes).

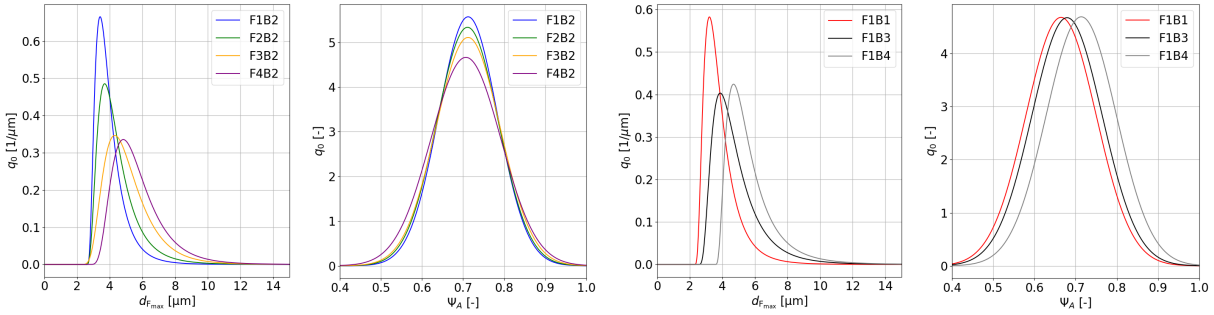

(a) Maximum Feret diameter (b) Aspect ratio (c) Maximum Feret diameter (d) Aspect ratio

Figure 8: PDFs of the fitted lognormal and normal distributions for granule size $d_{\mathrm{F_{max}}}$ (a) and aspect ratio Ψ_{A} (b) for F series, and corresponding PDFs of the fitted lognormal and normal distributions for B series (c,d).

Table 5: Model parameter values of fitted distributions for $d_{\mathrm{F_{max}}}$ and Ψ_{A}.

	$d_{\mathrm{F_{max}}}$		Ψ_{A}		
	μ	σ	μ	σ	c
F1B2	0.188	0.592	2.563	0.712	0.072
F2B2	0.520	0.577	2.487	0.711	0.075
F3B2	1.032	0.455	2.031	0.712	0.078
F4B2	1.037	0.471	2.572	0.707	0.086
F1B1	0.315	0.597	2.249	0.665	0.085
F1B3	0.687	0.594	2.476	0.679	0.085
F1B4	0.579	0.652	3.523	0.714	0.085

Prediction of descriptor distributions. By applying the regression procedure described in Section 2.8 to the F series and B series, we can predict the probability densities of descriptors for

process parameters, for which no measurements have been conducted yet. For both series and both considered granule descriptors $d_{\mathrm{F_{max}}}$ and Ψ_{A}, we fit the regression function g (see Eqs. (5) and (6)) to capture the relationship between the process parameters z (the feed rate in the F series and the binder concentration in the B series) and the model parameters θ of the corresponding probability densities of the conducted experiments. The resulting fit of the linear regressions can be observed in Figure 9 and Table 6. A high degree of agreement between the fitted regression lines and the model parameters can be observed.

With the fitted regression functions, we can predict the distribution of $d_{\mathrm{F_{max}}}$ and Ψ_{A} for intermediate feed rates or binder concentrations that we did not experimentally measure. More precisely, the regression function fitted to the data set belonging to the F series can be utilized to predict the model parameters of the distribution of $d_{\mathrm{F_{max}}}$ and Ψ_{A} for processes with arbitrary feed rate in $z \in [11, 20]$ and a fixed binder concentration of 0.8 wt%, whereas the regression functions fit to the B series can be utilized to predict the model parameters of the distribution of $d_{\mathrm{F_{max}}}$ and Ψ_{A} for arbitrary concentrations $z \in [0.8, 3.2]$ and a fixed feed rate of $11\,\mathrm{mL\,min^{-1}}$. By inserting the predicted model parameters $\theta = g(z)$ into Eqs. (7) and (8), we acquired predictions for the probability densities of granule descriptors, for which possibly no measurements have been conducted yet.

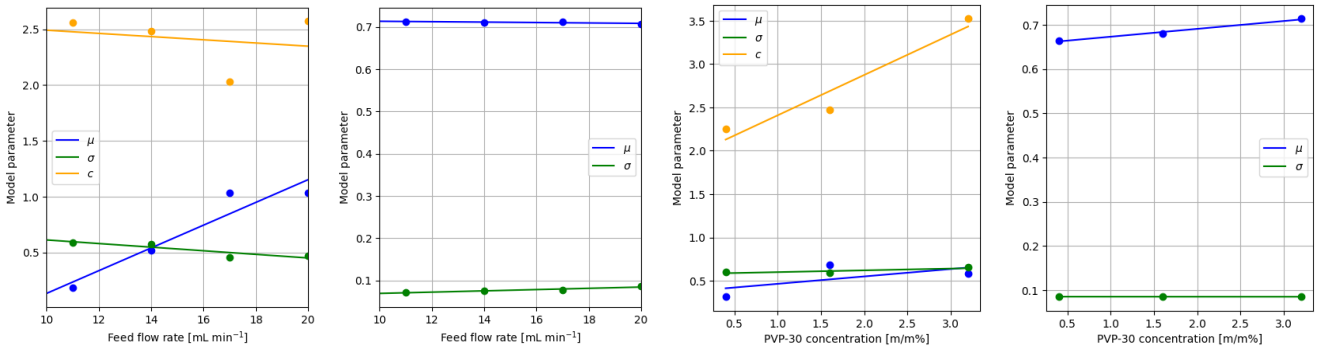

(a) (b) (c) (d)

Figure 9: Regression of model parameters for the lognormal distribution (a,c) and the normal distribution (b,d), where (a, b) correspond to F series, and (c, d) to B series.

Table 6: Regression parameter values of fitted functions.

		$d_{\mathrm{F_{max}}}$			Ψ_{A}	
		μ	σ	μ	σ	c
F series	**a**	0.102	-0.016	-0.014	0.000	0.002
	b	-0.886	0.774	2.636	0.718	0.054
B series	**a**	0.085	0.020	0.466	0.018	0.000
	b	0.379	0.579	1.942	0.6558	0.085

Before showing exemplary resulting predicted probability densities, we examine the linear correlation between the granule descriptors $d_{\mathrm{F_{max}}}$ and Ψ_{A}. To quantify this, we consider the empirical Pearson correlation coefficients (EPCC), which is given by

$$\mathrm{EPCC}(x, y) = \frac{\sum_{i=1}^{n}(x_i - \overline{x})(y_i - \overline{y})}{\sqrt{\sum_{i=1}^{n}(x_i - \overline{x})^2}\sqrt{\sum_{i=1}^{n}(y_i - \overline{y})^2}}, \tag{9}$$

where $\overline{x}$ and $\overline{y}$ are the means of the x_i and y_i values, respectively. In this case, x_i and y_i represent the maximum Feret diameter and aspect ratio of the i-th granule, respectively, from the SOPAT images. For the experiments F1B2, F2B2, F3B2, F1B1, F1B3, and F1B4, the EPCC has values close to 0 (EPCC < 0.02), indicating little to no linear correlation between the two descriptors. The observed near-zero EPCC values suggest that the size of the granules, as measured by $d_{\mathrm{F_{max}}}$, provides little information about their shape, as measured by Ψ_{A}, and thus, for simplicity we will neglect any modeling of their dependency.

Figure 10 displays the joint predicted probability densities for the maximum Feret diameter and aspect ratio, which are assumed to be independent random variables, for process parameters where no experimental data have been collected yet. In particular, in Figure 10 (middle column), these probability densities are shown for a feed rate of $12.5\,\mathrm{mL\,min^{-1}}$ and a binder concentration of 0.8 wt% (top row) as well as a feed rate of $11\,\mathrm{mL\,min^{-1}}$ and a binder concentration of 2.4 wt% (bottom row). Furthermore, Figure 10 shows the fitted densities for the experiments F1B2, F2B2, F1B3 and F1B4, along with their respective measured granule descriptors. Recall that the process parameters of these processes are shown in Table 1. The figure shows a high agreement of the fitted parametric probability densities with the displayed measured granule descriptors. Furthermore, in Figure 10, in both rows, a clear and desired shift in the location and variance of the distributions can be observed from left to right.

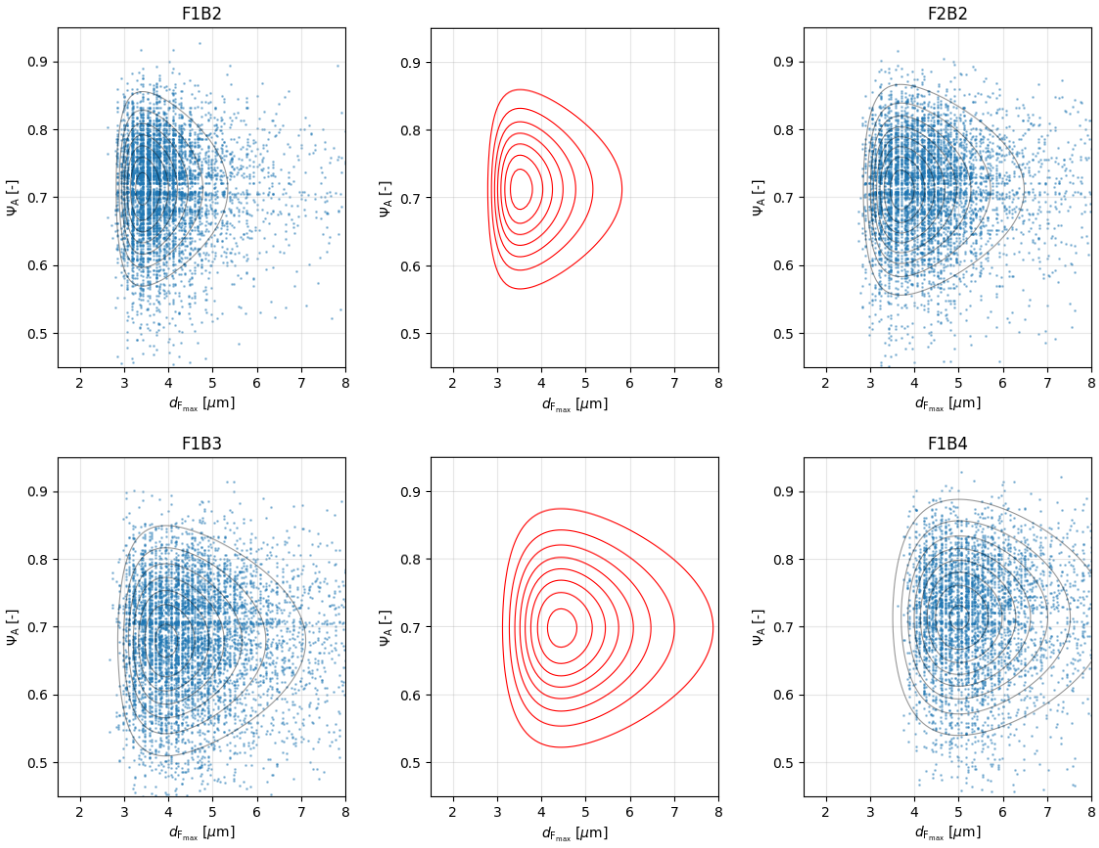

Figure 10: Bivariate descriptor distribution. The (parametric) bivariate distributions are shown as contour plots, together with corresponding measured data. The top row shows the effect of varying feed flow rates, whereas the bottom row shows the effect of varying binder concentrations. The red contours (middle column) arise from parameter interpolation for a feed rate of $12.5\,\mathrm{mL\,min^{-1}}$ and a binder concentration of 0.8 wt% (top row) as well as a feed rate of $11\,\mathrm{mL\,min^{-1}}$ and a binder concentration of 2.4 wt% (bottom row). Recall that we assumed independence of the maximum Feret diameter and aspect ratio when modeling their bivariate distribution.

In summary, we observed that the feed rate strongly controls the maximum Feret diameter distribution of granules (with higher feed rates yielding higher expected values and variances), while binder concentration influences both, the size and shape of the granules. In the following section, we will look into the inner structure of the granules using SEM.

3.3. SEM imaging of dried granules

To complement the in-line optical measurements, we examined the dried granules using off-line high-resolution SEM, which provides direct visual evidence of granule morphology and can reveal internal structural features (like hollow cores or pores) from broken granules. Figure 11 shows SEM images of granules produced in two experimental cases: F1B2 (low feed rate, 0.8 wt% binder) and F2B2 (high feed rate, 0.8 wt% binder), each imaged at two different magnifications.

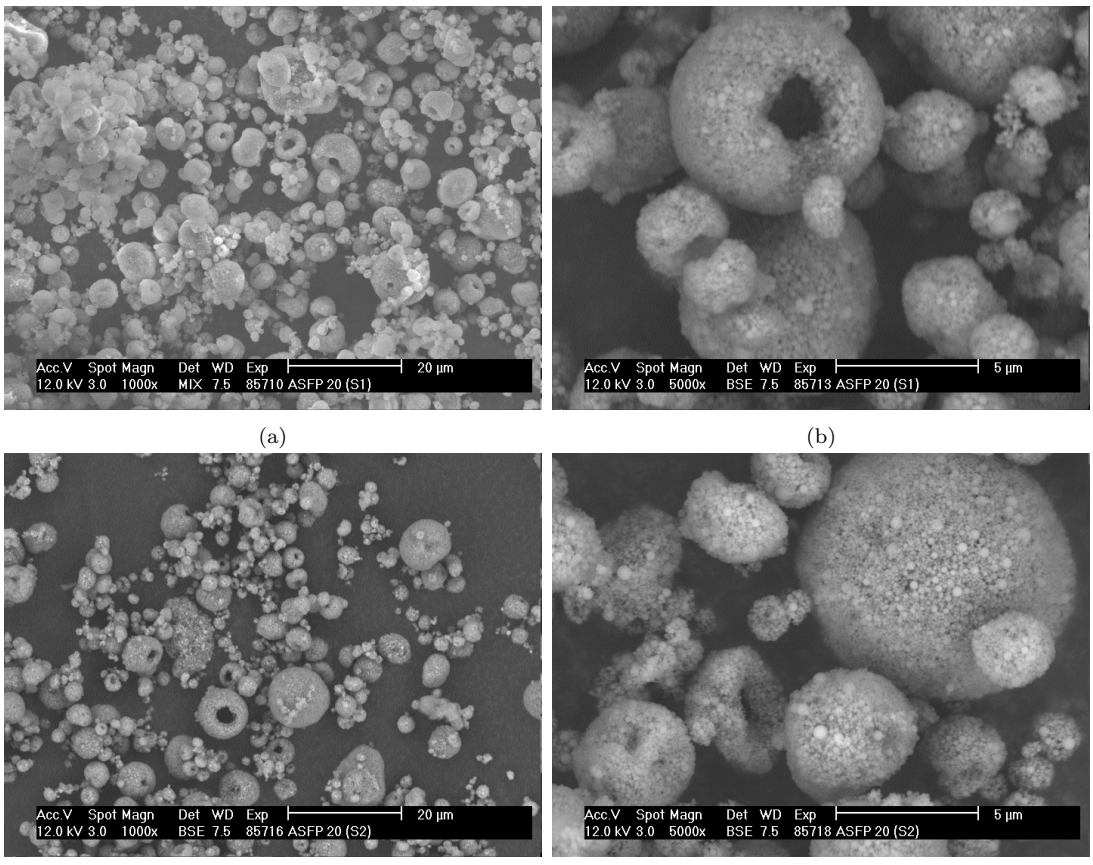

Figure 11: SEM images of spray-dried granules at two different feed rates: (a, b) low feed rate (F1B2), and (c, d) high feed rate (F2B2).

The SEM images confirm that the spray drying process produced composite granules consisting of alumina nano-particles dispersed in a PVP-30 matrix. The granules exhibit a variety of morphologies, predominantly spherical or near-spherical shapes, along with notable instances of doughnut-shaped granules and granules containing visible hollow cavities or surface depressions. In the lower-magnification views, F1B2 and F2B2 both show mostly individual spherical granules of a few microns in size.

At higher magnification, differences become apparent. Many granules have a doughnut-like morphology (ring-shaped or with a central pit). A fractured granule also reveals internal cracks and pores, indicating a porous interior structure. These features likely arise from the dynamics

between solvent evaporation and granule redistribution during the final stages of drying, discussed in detail in Section 4.4 below. Some granules, by contrast, exhibit relatively smooth surfaces and appear more solid. These observations collectively demonstrate the morphological variations ranging from uniformly dense to hollow and cracked porous structures, motivating a quantitative analysis of granule pore volume and pore size using mercury intrusion porosimetry, as discussed in the following section.

3.4. Granule porosity analysis

The 3D volume of pore space was measured using the PASCAL 440 (Thermo Fisher Scientific GmbH) mercury porosimeter for selected experimental cases to investigate how feed rate and binder concentration affect the pore structures. Measurements focused on samples produced at different feed rates under a constant binder concentration (F1B2 – F4B2) and on samples with varying binder concentrations (F1B1 and F1B2). For each measurement, a sample with a certain mass of the dried granules (m_{sample}) was taken and mercury was pressed into the sample. The sample was first subjected to an intrusion cycle from atmospheric pressure (101 325 Pa $\approx$ 0.1 MPa) up to 100 MPa. As the pressure increases, more mercury is forced into the pore space of the sample. The instrument sums up how much mercury has been intruded ($V_{intruded}$) at each pressure step, giving a total intruded volume for each pressure. After reaching 100 MPa, the pressure was released to 10 MPa. A second intrusion cycle then increased the pressure from 10 MPa to 400 MPa. Figure 12a shows the resulting specific volume of mercury intruded (normalized by the mass, $V_{intruded}/m_{sample}$) as a function of the applied pressure for the experimental cases mentioned above, where the intrusion-extrusion-intrusion cycle can be observed. A steep jump at relatively low pressure implies that the samples have a high fraction of macro-pores, which mainly are pores between individual granules. However, we are interested in the nano-pores (in the range of 10 nm - 150 nm) within the granules. By assuming that the pores behave like cylindrical capillaries, we can compute pore sizes corresponding to given pressures by means of the Washburn equation [48], which is given by

$$r_P = -\frac{2\gamma \cos\theta}{P}, \tag{10}$$

where r_p is the pore radius corresponding to the applied pressure p, γ ($= 480\,\mathrm{nN\,m^{-1}}$) is the surface tension of mercury, θ ($= 140°$) is the wetting angle.

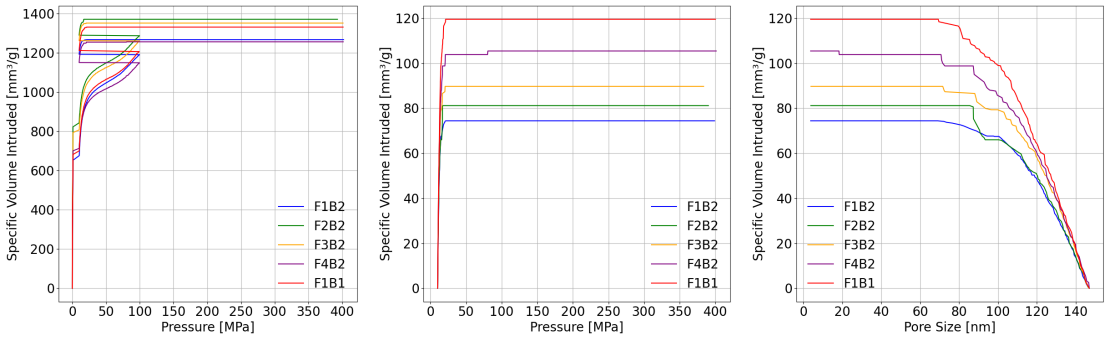

(a) (b) (c)

Figure 12: (a) Specific volume of mercury intruded versus applied pressure for the entire intrusion-extrusion-intrusion cycle (0.1 MPa → 100 MPa, 100 MPa → 10 MPa, 10 MPa → 400 MPa); (b) Specific volume of mercury intruded during the second intrusion cycle (10 MPa - 400 MPa); (c) Specific volume of mercury intruded during the second intrusion cycle as a function of pore sizes (10 nm – 150 nm), according to Eq. (10).

To focus on the nano-pores within the granules, we analyze only the specific volume intruded during the second intrusion cycle. This is achieved by subtracting for each experiment the specific volume already intruded after the first intrusion-extrusion cycle, see Figure 12b. We can observe that for higher feed rates, the specific volume intruded is higher, meaning that the total specific volume of the nano-pores is higher. Moreover, reducing the binder concentration leads to a higher total specific volume of nano-pores.

In Figure 12c, we changed the x-axis of Figure 12b to get an estimation of the specific volume of mercury intruded for given pore sizes, according to Eq. (10). Recall that increasing the feed rate and decreasing the binder content yields granules with higher specific mercury-intruded pore volumes. In Figure12c we can observe that these differences are primarily attributed to pores in the size range from 80 nm to 140 nm. In contrast, no significant differences are observed for pores with sizes less than 80 nm.

4. Discussion

4.1. Influence of process parameters on droplet characteristics

The spray drying experiments demonstrated the critical influence of feed rate and binder concentration on the initial droplet characteristics, notably size and velocity distributions. Reduced binder concentration at a constant low feed rate resulted in smaller and faster droplets, a phenomenon consistent with fundamental fluid mechanics. Lower viscosity liquids facilitate easier breakup into finer droplets due to decreased resistance during atomization, subsequently accelerating more readily in the airflow. Conversely, higher feed rates at constant binder concentration yielded larger droplets with increased velocities, reflecting enhanced momentum flux from the nozzle. Such conditions require more energy for atomization and therefore produce larger initial droplets. Understanding these initial droplet dynamics is crucial, as they directly influence subsequent drying mechanisms and ultimately determine the final properties of the granules.

4.2. Impact of droplet characteristics on granule morphology

The initial droplet characteristics influenced the resultant granule size and morphology. Higher feed rates consistently led to larger maximum Feret diameters in dried granules, a direct consequence of larger initial droplets entraining more solid material. Binder concentration, however, influenced granule morphology differently. At low binder concentrations, granules exhibited moderate size increases, primarily due to granule stabilization rather than extensive bridging. Conversely, higher binder concentrations increased granule sizes through enhanced polymer bridging of alumina nanoparticles into larger, coherent structures during the drying stage.

4.3. Parametric modeling and process optimization

Our study utilized parametric modeling to quantitatively describe granule descriptor distributions using regression functions linking process parameters to probability distribution parameters. These functions not only enable predictions of granule characteristics under untested intermediate conditions but also provide a systematic approach to process optimization. Specifically, given a desired distribution of maximum Feret diameters and aspect ratios, it is possible to identify optimal spray drying parameters by minimizing the discrepancy between predicted and target distributions.

Given the primary objective of this study — to present initial insights into the relationships between process parameters, granule morphology, and size — we intentionally limited our modeling analysis to qualitative visual assessments. Formal statistical validation of these predictive models was not conducted, as this would involve complex interpretations of parameter sensitivity and

advanced statistical metrics. Rigorous validation of these predictive models using formal statistical approaches will be an essential future step, employing appropriate metrics for enhanced model accuracy and interpretability.

Although negligible linear correlation between the maximum Feret diameters and aspect ratios justified our use of independent marginal distributions, our regression approach is sufficiently general to accommodate more complex multivariate descriptor vectors. Future investigations may beneficially integrate additional descriptors such as internal porosity or surface roughness. Advanced multivariate statistical tools, such as copulas [49], could manage the interdependencies among these descriptors effectively, enabling a more comprehensive understanding and control over granule quality.

The presented regression framework also allows for simultaneous exploration of multiple process parameters and their interactive effects. However, expanding the parameter space dimensionality necessitates significantly larger datasets to robustly calibrate multivariate regression functions. Consequently, future studies would prioritize extensive experimental datasets complemented by sophisticated statistical modeling to explore these higher-dimensional parameter interactions thoroughly.

4.4. Microstructural insights and implications

SEM imaging provided detailed insights into the granule morphologies formed under varying spray drying conditions, complementing the droplet size and velocity analyses. Granules exhibited frequent doughnut-like shapes and internal voids or cracks, indicating that rapid surface solidification and uneven internal solvent evaporation were key drivers in their formation. Conversely, the granules which demonstrated relatively uniform, dense, and smooth spherical structures were due to more uniform drying.

Specifically, doughnut-like structures emerged due to a rapid drying mechanism, wherein the outer layer solidifies quickly, causing internal solvents to escape unevenly and create internal voids [50]. Additionally, the presence of internal cracks in some granules suggests that drying-induced stresses during solvent evaporation and polymer shrinkage contribute to their porosity. Lower feed rate conditions, facilitating rapid and uniform solvent evaporation, minimize such stresses and thus result in more solid, spherical granules with smoother surfaces.

Mercury intrusion porosimetry results further substantiated these SEM observations. At higher feed rates, the resulting granules exhibited larger pore volumes, signaling more extensive internal voids and, consequently, an overall increase in granule porosity. This outcome may be attributed to the larger droplets formed under higher feed rates. Such droplets typically undergo rapid shell formation at the surface while retaining substantial liquid in the core. Once a visco-elastic skin or crust develops at the droplet perimeter, internal evaporation forces can inflate or maintain an enlarged interior cavity, ultimately leading to the higher specific pore volume observed [51]. Simultaneously, granules produced at lower binder concentrations showed significantly higher pore volumes owing to insufficient polymer bridging between the alumina nano-particles. When the polymer fraction is reduced, it becomes less capable of filling or reinforcing the interstitial spaces, thus preserving a comparatively open and porous internal architecture. By contrast, higher binder fractions effectively occupy and consolidate the voids within the forming granule. In these cases, the denser polymeric network restricts pore growth by exerting stronger cohesive forces and facilitating granule shrinkage, thereby decreasing the final pore volume. These findings emphasize the critical role of binder concentration and feed rate in tailoring granule porosity, which directly impacts practical application properties. Specifically, higher porosity may be beneficial for applications requiring increased surface area, such as catalysis or controlled drug release, but could adversely

affect mechanical strength and durability.

In summary, this investigation offers detailed micro-structural insights connecting spray drying conditions, droplet characteristics, and granule morphology. By systematically adjusting binder concentration and feed rate, we demonstrated the ability to manipulate granule micro-structures and thus tailor their physical properties for specific application needs.

5. Conclusion and outlook

This study provides a comprehensive analysis of the relationship between spray drying process parameters and the morphology of resulting alumina–polymer nanocomposite granules. By systematically varying the feed rate and binder (polymer) concentration and employing advanced characterization techniques, we elucidated the fundamental mechanisms governing granule size, morphology and porosity in the spray drying of nano-alumina/PVP suspensions.

In summary, we found that an increased feed rate leads to larger granules and higher granule pore volumes and sizes. Higher feed rates promote the formation of larger droplets at the nozzle, which in turn produce larger dried granules. These larger droplets also dry less uniformly, resulting in hollow or porous granules. SEM and mercury intrusion porosimetry consistently confirmed that granules produced at higher feed rates are larger and tend to form hollow or porous structures. Thus, feed rate emerges as a critical factor controlling not only granule size but also internal morphology (solid vs porous).

Conversely, a higher binder concentration (PVP-30 content) in the feed was found to produce more compact and less porous granules. With more binder present, the polymer fills the gaps between alumina nano-particles, leading to denser packing and fewer voids in the dried composite. The binder effectively acts as a "cement" that reinforces the granule structure. Additionally, higher binder concentrations tended to yield granules with slightly higher aspect ratios and smoother surfaces, as the polymer can form a continuous matrix around the alumina nano-particles.

The integration of in-line imaging with statistical distribution modeling in our work enabled us to not only measure the outcomes but also to develop predictive models for granule size and shape as functions of feed rate (and by extension, binder content). This model-based approach provides a potential framework for optimizing spray drying processes. For example, one could decide on a target granule size/shape descriptor distribution for a given application, and then use these empirical relationships to choose appropriate feed rates and binder concentrations to achieve those targets.

Future work will incorporate the building of a custom spray dryer equipped with advanced in-line sensors, enabling real-time monitoring and model-based control of granule formation processes. This spray dryer will integrate additional in-line pressure and temperature sensors for precise measurement of granule characteristics, providing crucial feedback for immediate adjustments of process parameters. Additionally, a dedicated preconditioning stage before atomization is also planned, to precisely control particle interactions, suspension viscosity, and stability, enhancing the control over granule structures. Future work would also extend our initial findings by integrating additional structural descriptors, employing rigorous statistical validations, and exploring more complex multivariate relationships among spray drying parameters, granule structure, and performance outcomes. Furthermore, the current parametric modeling framework will be enriched through advanced statistical learning methods, such as copula-based modeling and autoencoders, facilitating real-time process adjustments and robust control strategies under varying operational conditions. Together, these planned enhancements will facilitate the implementation of real-time, autonomous closed-loop control strategies, significantly advancing the reproducibility and quality of spray-dried alumina–polymer composites.

Author contributions

R.M. : Conceptualization, Formal Analysis, Investigation, Methodology, Software, Visualization, Writing-original draft, Writing-review. L.F. : Investigation, Visualization, Software, Writing-original draft, Writing-review. O.F. : Supervision, Writing-review. Y.S. : Investigation, Writing-review. S.A. : Supervision, Funding Acquisition, Writing-review. V.S. : Supervision, Funding Acquisition, Writing-review. U.P. : Supervision, Funding Acquisition, Writing-review.

Acknowledgments

The authors gratefully acknowledge funding by the German Research Foundation (DFG) within SPP 2364 under grants 504580586 and 504954383, and would like to thank Dr. Gert Schmidt from the Institute of Ceramics, Refractories and Composite Materials, TU Bergakademie Freiberg, for conducting the SEM characterization, Annett Kästner for conducting the mercury intrusion porosimetry measurements, Abhishek Prashant Singh, Shalini Rawat and Siddhi Kulkarni for assisting in the spray drying experiments and Dr. Lisa Ditscherlein for fruitful scientific discussions.

Competing interests

The authors declare no competing interests.

Data availability

Data will be made available upon reasonable request.

References

[1] X. D. Zhou, S. C. Zhang, W. Huebner, P. D. Ownby, H. Gu, Effect of the solvent on the particle morphology of spray dried pmma, Journal of Materials Science 36 (15) (2001) 3759–3768. doi:10.1023/a:1017982018651.

[2] H.-C. Schwarzer, W. Peukert, Experimental investigation into the influence of mixing on nanoparticle precipitation, Chemical Engineering & Technology 25 (6) (2002) 657. doi:10.1002/1521-4125(200206)25:6<657::aid-ceat657>3.0.co;2-5.

[3] F. Iskandar, L. Gradon, K. Okuyama, Control of the morphology of nanostructured particles prepared by the spray drying of a nanoparticle sol, Journal of Colloid and Interface Science 265 (2) (2003) 296–303. doi:10.1016/s0021-9797(03)00519-8.

[4] T. Banert, U. A. Peuker, Production of highly filled Fe3O4/PMMA nanocomposites by the spraying process., Chemie Ingenieur Technik 77 (3) (2005) 224–227. doi:10.1002/cite.200407079.

[5] D. Ciprari, K. Jacob, R. Tannenbaum, Characterization of polymer nanocomposite interphase and its impact on mechanical properties, Macromolecules 39 (19) (2006) 6565–6573. doi:10.1021/ma0602270.

[6] P. Dallas, V. Georgakilas, D. Niarchos, P. Komninou, T. Kehagias, D. Petridis, Synthesis, characterization and thermal properties of polymer/magnetite nanocomposites, Nanotechnology 17 (8) (2006) 2046–2053. doi:10.1088/0957-4484/17/8/043.

[7] P. Castrillo, D. Olmos, D. Amador, J. González-Benito, Real dispersion of isolated fumed silica nanoparticles in highly filled pmma prepared by high energy ball milling, Journal of Colloid and Interface Science 308 (2) (2007) 318–324. doi:10.1016/j.jcis.2007.01.022.

[8] S. Gyergyek, M. Huskić, D. Makovec, M. Drofenik, Superparamagnetic nanocomposites of iron oxide in a polymethyl methacrylate matrix synthesized by in situ polymerization, Colloids and Surfaces A: Physicochemical and Engineering Aspects 317 (1–3) (2008) 49–55. doi:10.1016/j.colsurfa.2007.09.035.

[9] M. Rudolph, U. A. Peuker, Coagulation and stabilization of sterically functionalized magnetite nanoparticles in an organic solvent with different technical polymers, Journal of Colloid and Interface Science 357 (2) (2011) 292–299. doi:10.1016/j.jcis.2011.02.043.

[10] S. Kirchberg, M. Rudolph, G. Ziegmann, U. A. Peuker, Nanocomposites based on technical polymers and sterically functionalized soft magnetic magnetite nanoparticles: Synthesis, processing, and characterization, Journal of Nanomaterials 2012 (1) (2012) 670531. doi:https://doi.org/10.1155/2012/670531.

[11] M. Rudolph, C. Turan, S. Kirchberg, G. Ziegmann, U. Peuker, Nanoparticles in organic solvents with polymers – stability and consequences upon material synthesis through spray drying and melt moulding, in: G. Tiddy, R. Tan (Eds.), NanoFormulation, The Royal Society of Chemistry, 2012, p. 177–187. doi:10.1039/9781849735247-00177.

[12] T. Banert, U. A. Peuker, Preparation of highly filled super-paramagnetic pmma-magnetite nano composites using the solution method, Journal of Materials Science 41 (10) (2006) 3051–3056. doi:10.1007/s10853-006-6976-y.

[13] M. Rudolph, J. Erler, U. A. Peuker, A TGA–FTIR perspective of fatty acid adsorbed on magnetite nanoparticles–decomposition steps and magnetite reduction, Colloids and Surfaces A: Physicochemical and Engineering Aspects 397 (2012) 16–23. doi:10.1016/j.colsurfa.2012.01.020.

[14] M. S. A. Darwish, U. Peuker, U. Kunz, T. Turek, Bi-layered polymer–magnetite core/shell particles: synthesis and characterization, Journal of Materials Science 46 (7) (2011) 2123–2134. doi:10.1007/s10853-010-5048-5.

[15] D. Santos, A. C. Maurício, V. Sencadas, J. D. Santos, M. H. Fernandes, P. S. Gomes, Spray drying: An overview, in: Biomaterials - Physics and Chemistry - New Edition, InTech, 2018. doi:10.5772/intechopen.72247.

[16] R. de Souza Lima, M.-I. Ré, P. Arlabosse, Drying droplet as a template for solid formation: A review, Powder Technology 359 (2020) 161–171. doi:https://doi.org/10.1016/j.powtec.2019.09.052.

[17] M. Rudolph, U. A. Peuker, Phase transfer of agglomerated nanoparticles: deagglomeration by adsorbing grafted molecules and colloidal stability in polymer solutions, Journal of Nanoparticle Research 14 (7). doi:10.1007/s11051-012-0990-6.

[18] C. Perecin, N. Cerize, V. Chitta, X. Gratens, P. Léo, A. de Oliveira, S. Yoshioka, Magnetite nanoparticles encapsulated with PCL and poloxamer by nano spray drying technique, Nanoscience and Nanotechnology 6 (4) (2016) 68–73. doi:10.5923/j.nn.20160604.03.

[19] H. Rothberg, S. Pietsch-Braune, L. Spahr, Y. Kanina, S. Heinrich, Production of magnetite-polyvinyl butyral composites using a nano spray dryer, Powder Technology 394 (2021) 394–402. doi:10.1016/j.powtec.2021.08.063.

[20] Z. Guo, T. Pereira, O. Choi, Y. Wang, H. T. Hahn, Surface functionalized alumina nanoparticle filled polymeric nanocomposites with enhanced mechanical properties, Journal of Materials Chemistry 16 (27) (2006) 2800. doi:10.1039/b603020c.

[21] S. Mallakpour, E. Khadem, Recent development in the synthesis of polymer nanocomposites based on nano-alumina, Progress in Polymer Science 51 (2015) 74–93. doi:10.1016/j.progpolymsci.2015.07.004.

[22] S. Hatamie, M. M. Ahadian, A. Rashidi, A. Karimi, O. Akhavan, Novel synthesis of cobalt/poly vinyl alcohol/gamma alumina nanocomposite for catalytic application, Applied Physics A 123 (5) (2017) 1–10. doi:10.1007/s00339-017-0913-6.

[23] S. Hossain, M. Hoque, Polymer nanocomposite materials in energy storage: Properties and applications, in: M. Jawaid, M. Mansoob Khan (Eds.), Polymer-based Nanocomposites for Energy and Environmental Applications, Elsevier, 2018, p. 239–282. doi:10.1016/b978-0-08-102262-7.00009-x.

[24] M. Pourmadadi, A. Farokh, E. Rahmani, A. Shamsabadipour, M. M. Eshaghi, A. Rahdar, L. F. R. Ferreira, Porous alumina as potential nanostructures for drug delivery applications, synthesis and characteristics, Journal of Drug Delivery Science and Technology 77 (2022) 103877. doi:10.1016/j.jddst.2022.103877.

[25] D. H. Huntington, The influence of the spray drying process on product properties, Drying Technology 22 (6) (2004) 1261–1287. doi:10.1081/drt-120038730.

[26] A. B. D. Nandiyanto, K. Okuyama, Progress in developing spray-drying methods for the production of controlled morphology particles: From the nanometer to submicrometer size ranges, Advanced Powder Technology 22 (1) (2011) 1–19. doi:10.1016/j.apt.2010.09.011.

[27] M. Homayoonfal, N. Malekjani, V. Baeghbali, E. Ansarifar, S. Hedayati, S. M. Jafari, Optimization of spray drying process parameters for the food bioactive ingredients, Critical Reviews in Food Science and Nutrition 64 (17) (2022) 5631–5671. doi:10.1080/10408398.2022.2156976.

[28] S. Höhne, V. Gaukel, Impact of the drying rate on product properties of spray dried emulsions to enable a targeted product design, Drying Technology 42 (14) (2024) 2080–2086. doi:10.1080/07373937.2024.2306525.

[29] J. Nicklas, U. Peuker, Agglomeration of fine hydrophobic particles: 1D and 2D characterization by dynamic image analysis of in-line probe data, Powder Technology 426 (2023) 118685. doi:10.1016/j.powtec.2023.118685.

[30] N. Eiermann, O. Furat, J. Nicklas, U. Peuker, V. Schmidt, Quantitative characterization of hydrophobic agglomeration at different mixing intensities using a copula-based probabilistic modeling approach, Powder Technology (in print).

[31] T. Allen, Mercury porosimetry, in: Particle Size Measurement, Springer, 1990, p. 653–681. doi:10.1007/978-94-009-0417-0_19.

[32] D. E. Dobry, D. M. Settell, J. M. Baumann, R. J. Ray, L. J. Graham, R. A. Beyerinck, A model-based methodology for spray-drying process development, Journal of Pharmaceutical Innovation 4 (3) (2009) 133–142. doi:10.1007/s12247-009-9064-4.

[33] L. N. Petersen, N. K. Poulsen, H. H. Niemann, C. Utzen, J. B. Jørgensen, Comparison of three control strategies for optimization of spray dryer operation, Journal of Process Control 57 (2017) 1–14. doi:10.1016/j.jprocont.2017.05.008.

[34] J. M. Schmitt, J. M. Baumann, M. M. Morgen, Predicting spray dried dispersion particle size via machine learning regression methods, Pharmaceutical Research 39 (12) (2022) 3223–3239. doi:10.1007/s11095-022-03370-3.

[35] L. N. Petersen, N. K. Poulsen, H. H. Niemann, C. Utzen, J. B. Jørgensen, Comparison of linear and nonlinear model predictive control for optimization of spray dryer operation, IFAC-PapersOnLine 48 (23) (2015) 218–223. doi:10.1016/j.ifacol.2015.11.286.

[36] C. A. Muñoz López, K. Peeters, J. Van Impe, Data-driven modeling of the spray drying process. process monitoring and prediction of the particle size in pharmaceutical production, ACS Omega 9 (24) (2024) 25678–25693. doi:10.1021/acsomega.3c08032.

[37] M. Neumann, P. Gräfensteiner, C. Santos de Oliveira, J. Martins de Souza e Silva, S. Koppka, D. Enke, P. Huber, V. Schmidt, Morphology of nanoporous glass: Stochastic 3d modeling, stereology and the influence of pore width, Phys. Rev. Mater. 8 (2024) 045605. doi:10.1103/PhysRevMaterials.8.045605.

[38] B. Prifling, D. Westhoff, D. Schmidt, H. Markoetter, I. Manke, V. Knoblauch, V. Schmidt, Parametric microstructure modeling of compressed cathode materials for Li-ion batteries, Computational Materials Science 169 (2019) 109083. doi:10.1016/j.commatsci.2019.109083.

[39] O. Furat, M. Masuhr, F. E. Kruis, V. Schmidt, Stochastic modeling of classifying aerodynamic lenses for separation of airborne particles by material and size, Advanced Powder Technology 31 (6) (2020) 2215–2226. doi:10.1016/j.apt.2020.03.014.

[40] H. Koivuluoto, V. Matikainen, J. Larjo, P. Vuoristo, Novel online diagnostic analysis for in-flight particle properties in cold spraying, Journal of Thermal Spray Technology 27 (3) (2018) 423–432. doi:10.1007/s11666-018-0685-3.

[41] B. Silverman, Density Estimation for Statistics and Data Analysis, Routledge, 2018. doi:10.1201/9781315140919.

[42] S. A. Villar, S. Torcida, G. G. Acosta, Median filtering: A new insight, Journal of Mathematical Imaging and Vision 58 (1) (2016) 130–146. doi:10.1007/s10851-016-0694-0.

[43] S. Pizer, R. Johnston, J. Ericksen, B. Yankaskas, K. Muller, Contrast-limited adaptive histogram equalization: speed and effectiveness, in: Proceedings of the First Conference on Visualization in Biomedical Computing, 1990, pp. 337–345. doi:10.1109/VBC.1990.109340.

[44] C. Tomasi, R. Manduchi, Bilateral filtering for gray and color images, in: Proceedings of the Sixth International Conference on Computer Vision (IEEE Cat. No.98CH36271), ICCV-98, Narosa Publishing House, 1998, p. 839–846. doi:10.1109/iccv.1998.710815.

[45] N. Otsu, A threshold selection method from gray-level histograms, IEEE Trans. Syst. Man Cybern. 9 (1979) 62–66. doi:10.1109/TSMC.1979.4310076.

[46] J. Shao, Mathematical Statistics, Springer, 2008. doi:10.1007/b97553.

[47] N. L. Johnson, S. Kotz, N. Balakrishnan, Continuous Univariate Distributions, Vol. 2, J. Wiley & Sons, 1995.

[48] E. W. Washburn, Note on a method of determining the distribution of pore sizes in a porous material, Proceedings of the National Academy of Sciences 7 (4) (1921) 115–116. doi:10.1073/pnas.7.4.115.

[49] R. B. Nelsen, An Introduction to Copulas, Springer, 2006. doi:10.1007/0-387-28678-0.

[50] P. Biswas, D. Sen, S. Mazumder, P. Doshi, Controlling sphere to doughnut transformation during quick drying of colloidal micrometric droplets, AIP Conference Proceedings 1832 (1) (2017) 140009. doi:10.1063/1.4980791.

[51] I. Siemons, R. Politiek, R. Boom, R. van der Sman, M. Schutyser, Dextrose equivalence of maltodextrins determines particle morphology development during single sessile droplet drying, Food Research International 131 (2020) 108988. doi:https://doi.org/10.1016/j.foodres.2020.108988.